Catalysis Letters (2020) 150:2660–2673
https://doi.org/10.1007/s10562-020-03142-x

Double Catalyst-Catalyzed: An Environmentally Friendly Sustainable Process to Produce Methallyl Alcohol

Fangfang Shang[1] · Qingyan Chu[1] · Haiyu Yang[1] · Haoxuan Yu[1] · Tonghe Diao[1] · Ping Wang[1] · Hui Liu[1] · Ming Wang[1]

Received: 2 December 2019 / Accepted: 11 February 2020 / Published online: 6 March 2020

Abstract

A green, sustainable process route to produce methallyl alcohol via tandem reaction concluding α-H oxidation, esterification and hydrolysis reaction is discussed. Pd–Au bimetallic nanocatalysts over SiO_2 mixed oxides incorporating K^{2+} and Al^{3+} like promoters were prepared by equivalent volume impregnation, which is using catalyzed the tandem reaction. Homo-dispered $ZnO–S_2O_8^{2-}$ nanoparticles supported on ZSM-5 were prepared by ultrasonic adsorption method, which is using catalyzed hydrolysis reaction. Characterization by transmission electron microscopy confirmed that alloyed Pd/Au nanoparticles with a mean diameter of 0.5 to 1.0 nm were formed. The results of X-ray diffraction confirmed that the crystal structure were Pd/Au(111). The electronic effect and geometric effect of Pd/Au significantly improved the catalytic performance. The effects of reaction pressure, temperature, and ratio of material were discussed in details. The catalytic activity of $ZnO–S_2O_8^{2-}$/ZSM-5 exhibited more excellent than H_2SO_4 and other reported catalysts with 100% conversion and selectivity. The excellent catalytic activity of $ZnO–S_2O_8^{2-}$/ZSM-5 may be attributed to the synergistic effect from the nano-effect of $ZnO–S_2O_8^{2-}$ nanoparticles and the mesostructure of ZSM-5, and the pore size, number of Brönsted acid sites. The reaction temperature are critical factors affecting the catalytic activity for this system. Based on the results, a supposed mechanism of the tandem and hydrolysis reaction was proposed.

Graphic Abstract

Atom economic green reaction: acetyl oxidation and hydrolysis reaction.

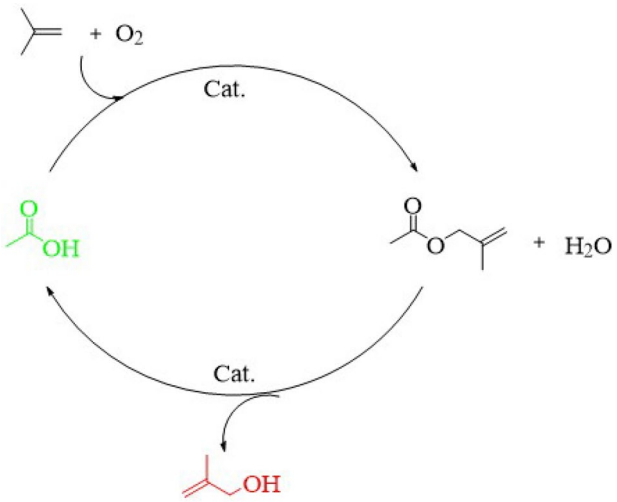

Electronic supplementary material The online version of this article (https://doi.org/10.1007/s10562-020-03142-x) contains supplementary material, which is available to authorized users.

Extended author information available on the last page of the article

Keywords Pd–Au/SiO_2 · Methallyl alcohol · Oxygen acylation · Nanoparticle · ZnO–$S_2O_8^{2-}$/ZSM-5 · Hydrolysis

1 Introduction

Circular Economy has emerged as a current research topic that is shaping public policy in America, Europe and elsewhere [1, 2], which is based on the natural cycle and evidences a perfectly balanced operation. In the circular economy, there is no such thing as waste, because it becomes a new source of resources, which, if possible, should promote value to the new product [3]. Methallyl alcohol has been being applied in industrial products and food fields as the intermediate substance and additive [4, 5]. Especially, it is used for the new generation of high-performance concrete super plasticizers raw material-methyl allyl polyoxyethylene ether [6], which has a promising market. At the end of the 12th 5-year plan [7, 8], the demand for concrete admixtures only in the field of methylallyl polyoxyethylene ether will reach 236,600 t, and the annual demand for methylallyl alcohol will reach 10,000 t. Meanwhile, methallyl alcohol replaces the toxic allyl alcohol to produce polycarboxylate cement superplasticizer [9], which makes the market prospect of methyl allyl alcohol more clear.

Traditional methods of the methallyl alcohol synthesis relied on the hydrolysis of isobutene chloride with alkaline conditions or on the selective hydrogenation of methylacrolein. The first method refers to the process where chlorination of isobutene to synthetic isobutene chloride, which is hydrolyzed under alkaline conditions to generate methallyl alcohol, described as Scheme 1a. The method is the most widely used technical route in most of the countries all over the world. However, the method has drawbacks of low selectivity and yield, meanwhile by-product high salt wastewater. For the last method, isobutene is oxidized to methylacrolein, which is hydrogenated to methallyl alcohol, described as Scheme 1b. Although this method can be realized in terms of reaction principles and forces, the first step involves a large number of side reactions, resulting in low selectivity of methylacrolein. Due to the presence of double bonds and aldehyde groups, selective hydrogenation of the aldehyde group is required, resulting in low selectivity and high total production and construction costs. The industrial applications of these methods still limited due to the time consuming (multi-steps to remove the by-products), high cost and high pollution. Therefore, it is necessary to develop a simple, efficient and green synthesis route of methallyl alcohol.

Numerous reports are available on the synthesis of vinyl acetate and allyl acetate from ethylene by oxygen acylation [10, 11], which inspires our research. The preparation of carboxylate by olefin acetylation is a process that combines olefin α-H oxidation and esterification, which represents the development trend of unsaturated olefin carboxylate synthesis technology. Methallyl alcohol was prepared by hydrolysis of isobutene acetate. In this paper, we have prepared Pd–Au bimetallic nanoparticles supported on SiO_2 with core–shell structure by constant volume impregnation method, which is using catalyzed the tandem reaction of oxygen acylation. Traditionally, carboxylate is hydrolyzed to synthesize alcohol via Brønsted bases in order to achieve higher yields, which produces a amount of waste salt. Therefore, we developed homo-dispered ZnO–$S_2O_8^{2-}$ nanoparticles supported on ZSM-5 (ZnO–$S_2O_8^{2-}$/ZSM-5) by ultrasonic adsorption method [12, 13]. The hydrolysis reaction of carboxylate is carried through the neutral catalyst successfully with conversion and selectivity 100%. The reaction run by this method meets the principles of circular economy [14, 15]: the raw

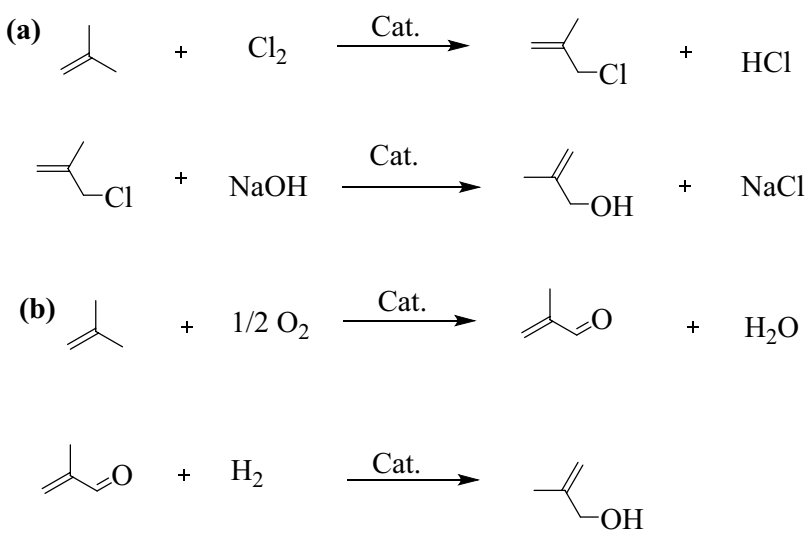

Scheme 1 The reaction of synthesis of methallyl alcohol

material-acetic acid could be recycled from the final products and the H_2O (by-products) could be using efficiently.

2 Experimental

2.1 Preparation of Catalysts and Its Characterizations

Sodium silicate (98%), Potassium acetate (98%), Palladium acetate (98%), gold acetate (98%), $Zn(NO_3)_2{\cdot}6H_2O$ (98%) and $(NH_4)_2S_2O_8$ were analytical and purchased from SINOPHARM Chemical Reagent Co., Ltd. SiO_2 spheres and ZSM-5 were obtained by Nanjing KFNANO Materials Tech Co., Ltd.

Pd–Au/SiO_2 core–shell catalyst was prepared by a method of constant volume impregnation. SiO_2 spheres, palladium acetate, gold acetate were used as raw materials, whereas sodium silicate was used as the agent which could convert Pd^{2+} into $Pd(OH)_2$. The potassium acetate was used as the promoted agent. The catalyst was drying at 120 °C for 24 h, and calcined at 500 °C for 6 h in a hydrogen atmosphere.

The $Zn(NO_3)_2$ aqueous solution was slowly added to the ZSM-5, then the mixture was evenly dispersed in an ultrasonic cleaner for 15 min. The mixture was dried at 45 °C for 12 h, and calcined at 350 °C for 6 h to get the ZS. A $(NH_4)_2S_2O_8$ aqueous solution was slowly added to the ZnO/ZSM-5 to afford $(NH_4)_2S_2O_8$-ZnO/ZSM-5, which was also dried at 45 °C for 12 h, and calcined at 300 °C for 6 h. During the process of calcinations, the temperature was increased at the rate of 1 °C/min, starting from 50 °C.

The characterizations of the catalysts were performed using the conventional techniques. Their morphology, chemistry, and crystal structure were characterized as the nanoscale. The samples were measured st room temperature with Cu $K_{\alpha1}$ radiation in the 2θ range of 5° to 90° using a STADI P automated transmission diffractometer (Ultima IV) equipped with a linear PSD (XRD). The chemical composition of the catalysts was established by means of X-ray fluorescence spectroscopy (XRF) on a VRA 30 spectrometer. The surface morphology of the catalysts were observed using a FEI Sirion 200 field-emission scanning electron microscope (SEM). TEM micrographs were recorded with a CM20 microscope (FEI) equipped with a STwin and LaB_6, at 200 kv. For EDX measurements without internal standard a PV9900 analyzer (EDAX) was used with spot sizes of approximately 50 nm. The X-ray photoelectron spectroscopy (XPS) measurements were recorded on a Thermo ESCALAB 250XI system with Mg K_α radiation (E = 1253.6 eV). The Fourier transform infrared (FT-IR) spectra were performed on a Nicolet 360 FT-IR instrument in the 4000–400 cm^{-1} region. N_2 adsorption–desorption isotherms and specific surface areas were measured at − 196 °C using a Micromeritics ASAP 2020 surface area and porosity analyzer. The infrared spectra of absorbed pyridine (pyridine-IR spectra) were gained on a PE Frontier FT-IR spectrometer.

2.2 Application System

The application system, shown schematically in Scheme 2, concludes mainly five parts: the feeding system, the preheating system, the reaction system, the heating and condensation system as well as the control and security system. The two metering pumps (Beijing Chuangxin Tongheng Science & Technology Co. Ltd. China) were used to feed separately CH_3COOH and isobutene, and the circulation pump (HANGZHOU Alkali Pump Co., Ltd. China) was used for the reaction medium loop. The gas flowing into the reactor was controlled by a gas pressure regulator device to adjust the pressure. The reactor was made from 316 L stainless steel, which concludes a fixed bed and jacket heat exchanger. The temperature of bed was adjusted by changing the flowrate of the outer oil circulation. The gas–liquid–solid three-phase system inside the draft tube followed downwards and was uniformly dispersed in the bed due to the fluxion of gas–liquid, increasing the efficiency of the reaction. The unreacted gas rose from the bottom and was re-dispersed with the liquid–solid binary phase by the sucking action. The reaction solution was filtered by a separator. Meanwhile, reactive mother liquor and the catalyst, were continuously recycled, feedstocks were continuously added into the system.

2.3 Synthesis of Methallyl Alcohol

The synthesis of methallyl alcohol was carried out in the reaction system according to the equation shown in Scheme 3. The reaction system concludes two parts: acetyl oxidation and ester hydrolysis. As shown in Scheme 2, the applied system was filled twice with N_2 and three times with O_2, and a set number of catalysts were filled in the bed of the reactor. Then, known amounts of CH_3COOH and isobutene were added by the circulation pump. The materials were heated to the desired temperature by preheater. N_2 gas was added into the reactor to maintain the system pressure, meanwhile, it could be diluted the reaction gas to enhance the safety factor. When the temperature of the bed reached the desired value, the CH_3COOH, isobutene and O_2 were fed continuously into the reaction system at a constant floe rate and fixed ratio. For the ester hydrolysis, the feedstock pump (Beijing Chuangxin Tongheng Science & Technology Co. Ltd. China) was used to feed water. The known amounts of reaction solution and water were added to the system. And the catalyst was filled in the bed, the products were collected in a 27 L tank and analyzed by gas chromatography.

Scheme 2 The diagram of industrial production process

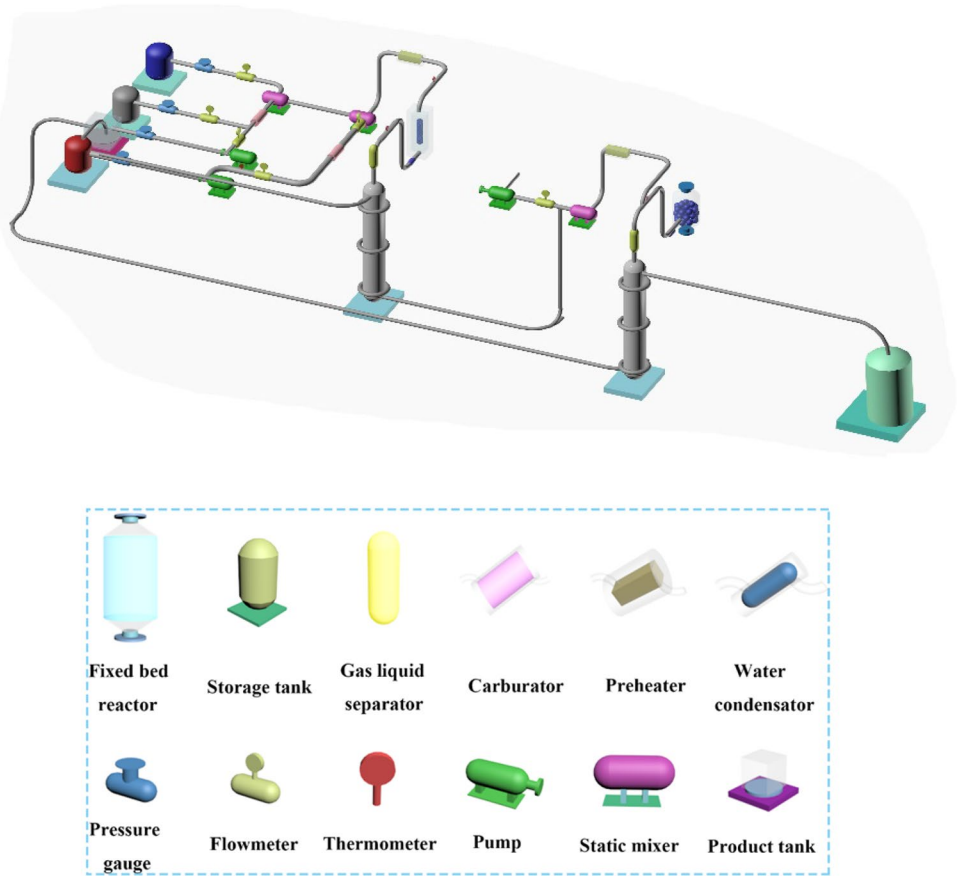

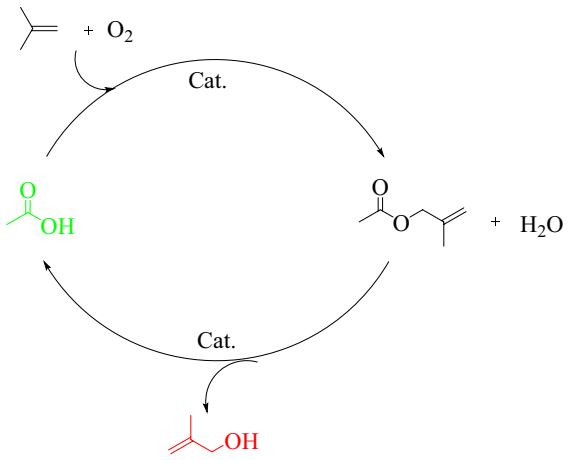

Scheme 3 The reaction of synthesis of methallyl alcohol

2.4 The Analysis of Product

The quantitative analysis of isobutene acetate was performed chromatographically (Agilent Technologies 7820A GC system, Palo Alto, CA, USA) on a Chrom 5 apparatus equipped with a flame-ionization detector (FID) and using a column packed with Chromosorb 101. The column temperature was programmed: isothermally 50 °C for 1 min, followed by an increase at the rate 5 °C/min, isothermally 200 °C for 5 min, then increased at the rate 20 °C/min, isothermally 220 °C for 15 min, and finally cooled to 50 °C. The quantitative analysis was performed by the external standard method.

3 Results and Discussion

3.1 Catalyst Characterization

The morphology of Pd–Au/SiO_2 was characterized by SEM and TEM. The TEM images were used to determine the individual size and morphology of the appropriate Pd–Au nanoparticles. As shown from Fig. 1b–d, the particle sizes were lower than 10 nm, besides, the lattice structure could be seen clearly. We can find that almost regular spherical shaped nanoparticles were formed. Moreover, the alloyed structure of the received nanoparticles could be confirmed by the XRD (Fig. 2a). The EDS results from selected TEM analyses are showed in Fig. 1f. It could be seen that the four main elements of Pd, Au, Si and O were uniformly distributed in the prepared catalytic material, which displayed the active components were equably dispersed in SiO_2. Furthermore,

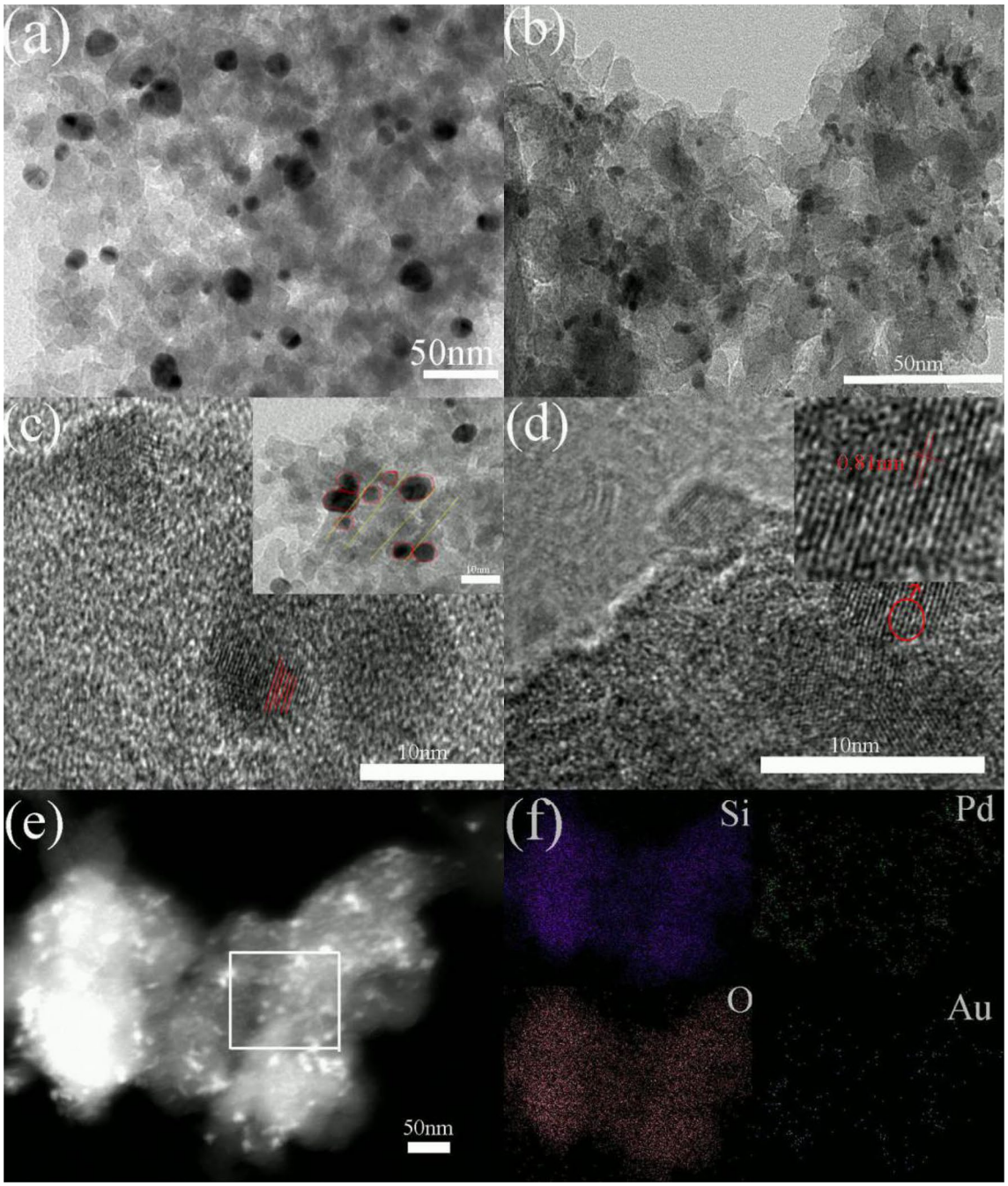

Fig. 1 **a** SEM images of Pd–Au/SiO_2; **b–d** TEM images of Pd–Au/SiO_2; TEM images (**e**) and elemental mapping (**f**) of the composite Pd–Au/SiO_2

the results of XRF presented the element content was 50.6% O, 41.3% Si, 2% Pd and 1% Au.

The crystallinity of the synthesized catalyst was characterized by XRD analysis showed in Fig. 2a. The results showed the expected reflexes of a Pd/Au(111) at 38° and 40°, whose diffraction peaks could be indexed to fcc Pd nanocrystal structure (JCPDS-05-681), fcc Au nanocrystal structure (JCPDS-04-0784). Figure 2b presented the survey XPS spectrum of Pd–Au/SiO_2, which indicated the existence of Pd, Au and K except to the elements of SiO_2 support (Si, O, N). The Pd 3d and Au 4f XPS spectra of Pd–Au/SiO_2 were given in Fig. 2c and d. The inspection of Pd 3d spectrum displayed the presence of metallic Pd (Pd^0 with Pd $3d_{5/2}$ at 335.7 eV and Pd $3d_{3/2}$ at 341.2 eV) [16, 17], the positive shift for Pd $3d_{5/2}$and Pd $3d_{3/2}$ could be attributed to the change of surface electronic state. Meanwhile, the inspection

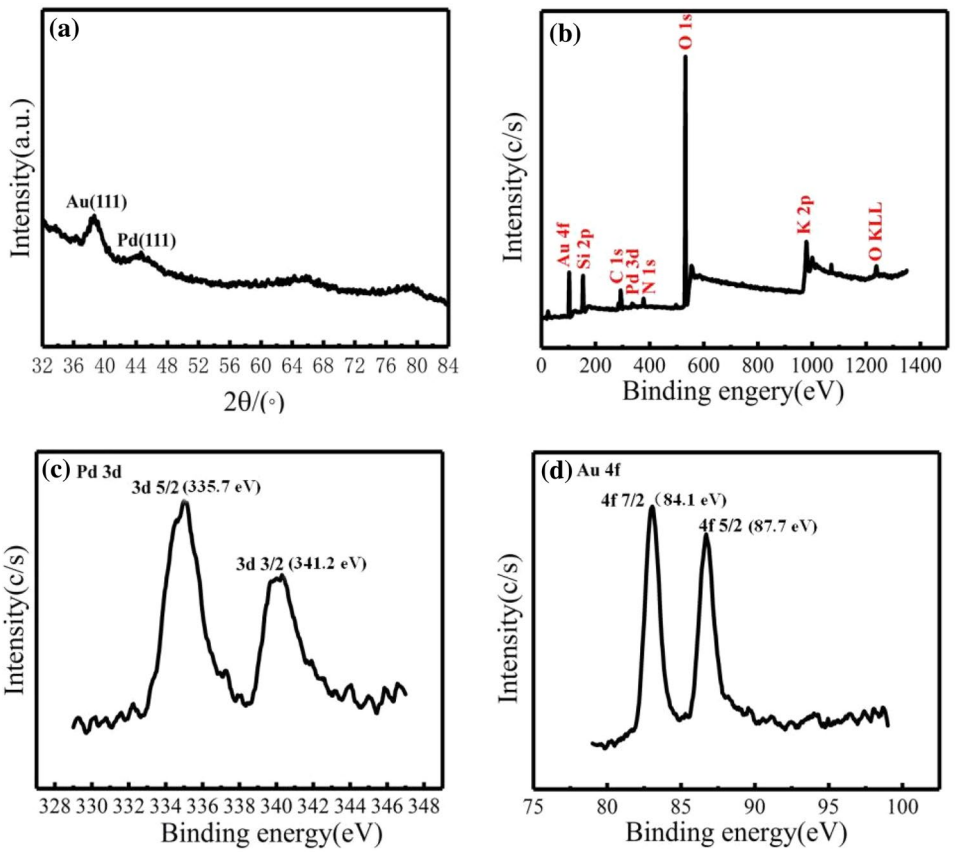

Fig. 2 **a** XRD of Pd–Au/SiO_2; **b** survey XPS spectrum; **c** Pd 3d XPS spectrum; **d** Au 4f XPS spectrum

of Au 4f spectrum revealed the presence of Au (Au^0 with Au $4f_{7/2}$ at 84.1 eV and Au $4f_{5/2}$ at 87.7 eV). XRD pattern of Pd–Au/SiO_2 exhibits a new diffraction peak located between the characteristic Pd and Au diffraction features, suggesting the formation of alloy structure.

Figure 3a and b show SEM images of ZnO–$S_2O_8^{2-}$/ZSM-5, giving almost uniform hexagonal-prisms, a typical morphology of MFI crystals, which indicates the morphology is virtually unaltered even after the loading of ZnO–$S_2O_8^{2-}$. It can be explained that the catalysts ZnO–$S_2O_8^{2-}$/ZSM-5 (average pore size of 2.5–5.0 nm) are easily aggregated to form nanoparticles and hence, the loading of ZSM-5 with ZnO–$S_2O_8^2$ did not alter the physical morphology of the ZSM-5 catalyst. The element mapping images (Fig. 3c) and the corresponding energy dispersive X-ray (EDX) data (Fig. 3d) confirm the existence of S and Zn element and various elements of Si, O, Zn and S are homogeneously distributed in the sample ZnO–$S_2O_8^{2-}$/ZSM-5.

The Fig. 4a shows the FT-IR spectra of ZSM-5 and ZnO/ZSM-5. The band of at 1095 cm^{-1} was related to the characteristic antisymmetric stretching vibration of Si–O–Si of ZSM-5 [18, 19]. The peaks at 798 and 466 cm^{-1} were assigned to the symmetric stretching vibration of Si–O [20]. It was apparent that the adsorption band at 798 cm^{-1} moved to 796 cm^{-1} after loading ZnO on ZSM-5. This effect was attributed to the stretching vibration of Si–O being perturbed by Zn^{2+} in a neighboring position. The FT-IR spectra of ZnO/ZSM-5 and ZnO–$S_2O_8^{2-}$/ZSM-5 are shown in Fig. 4b. Compared with ZnO/ZSM-5, ZnO–$S_2O_8^{2-}$/ZSM-5 showed the emergence of new bands in the range of 900–1300 cm^{-1}, which were attributed to the S=O or S–O bonds in the structures of the catalyst [21, 22]. In this range, the peaks at 1113 and 1127 cm^{-1} were assigned to the symmetric stretching vibration of S–O [23]. Meanwhile, the band at 1227 cm^{-1} was assigned to the stretching vibration of S=O [24]. The attribution of the characteristic vibration peaks was in keeping with the reported $S_2O_8^{2-}$ ion [25, 26]. Meanwhile, the characteristic stretching vibration of ZSM-5 is still existed. The results indicated the successful loading of ZnO–$S_2O_8^{2-}$ nanoparticles on the ZSM-5. Figure 4c showed the XRD patterns of ZSM-5 and ZnO/ZSM-5. The XRD diffraction patterns showed peaks at 2θ = 7.9, 8.7 22.9, 23.6 and 24.3° corresponding to ZSM-5, according to the literature [27, 28]. Three new peaks appeared in the diffraction pattern of ZnO/ZSM-5 after $Zn(NO_3)_2$ adsorption and calcination. The three peaks at 2θ = 31.8, 34.5, 36.1° corresponding ZnO [29, 30]. The XRD pattern of ZnO–$S_2O_8^{2-}$/ZSM-5 was similar to the ZnO/ZSM-5. However, six new peaks at 2θ = 14.7, 20.2, 21.5, 24.7, 29.7 and 32.5° were matched with the standard ICPDS card No. 33-0679 (Fig. 4d).

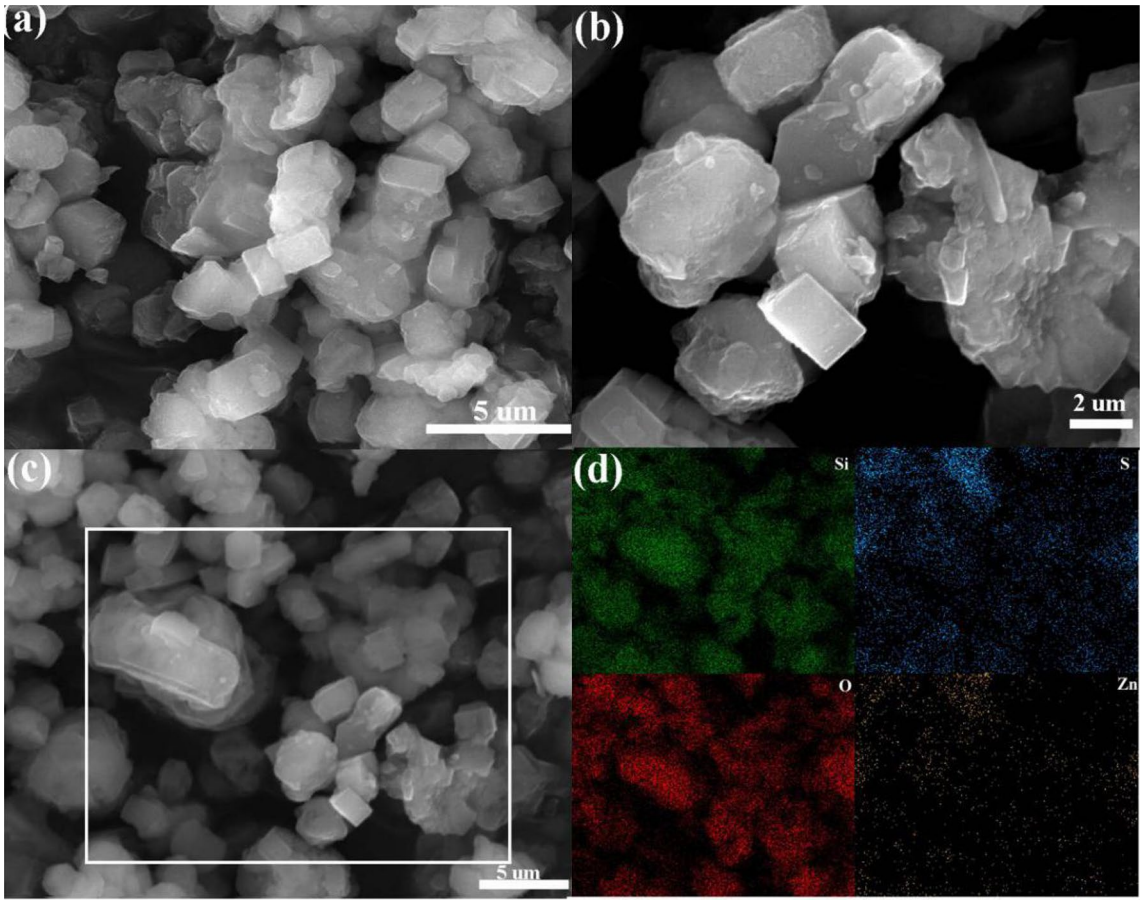

Fig. 3 **a–c** SEM images of ZnO–$S_2O_8^{2-}$/ZSM-5 and elemental mapping **d** of the composite

The aim of XPS measurements (Fig. 5a and b) is to investigate the chemical states of Zn and S in the sample. The Zn 2p spectra showed two peaks at 1021.9 eV and 1045.1 eV, which could be assigned to the Zn^{2+} species [31, 32]. The S^{6+} species was revealed by the binding energy at 169 eV, according to the literature [33]. N_2 adsorption desorption isotherms of ZnO–$S_2O_8^{2-}$/ZSM-5 were highlighted in Fig. 5c. According to IUPAC classifications and the literature [34], the isotherms showed a Type IV pattern, which exhibited a clear loop (H1 hysteresis loop) in the relative pressure range of 0.8–1.0. Hysteresis loops produced by capillary condensation indicate the presence of regular mesoporous channels in the material. Furthermore, we can confirmed that ZnO–$S_2O_8^{2-}$/ZSM-5 sustained the intact and ordered mesoporous structure of ZSM-5 after ZnO–$S_2O_8^{2-}$ loading. The textural characteristics of ZSM-5, ZnO–$S_2O_8^{2-}$ and ZnO–$S_2O_8^{2-}$/ZSM-5 were shown in Table 1. We can confirm that the BET surface area and pore volume of ZnO–$S_2O_8^{2-}$/ZSM-5 were obviously larger than ZnO–$S_2O_8^{2-}$.

The Py-IR spectra were employed to evaluate the types and intensity of Brönsted and Lewis acid sites of the catalyst [35, 36]. The pyridine-IR spectra (Fig. 5d) exhibited bands at 1439 and 1614 cm^{-1}, which proved the presence of Lewis acid sites in the catalyst. And the band at 1540 cm^{-1} was the characteristic of the pyridinium ion, which demonstrated the existence of Brönsted acid sites. The band at 1490 cm^{-1} was a combination between two separate bands at 1439 and 1540 cm^{-1}, which correspond to Brönsted and Lewis acid sites, respectively. Moreover, the changes of Brönsted acidity and Lewis acidity were observed at different desorption temperatures (50, 150 and 250 °C). In addition, the Brönsted acidity reduced more rapidly than the Lewis acidity with the temperature rising.

3.2 Synthesis of Isobutene Acetate

A series of palladium-based catalysts (Pd–Cu/SiO_2, Pd–Au/SiO_2, Pd–Te/SiO_2, Pd–Cd/SiO_2) were prepared and the catalytic activities were evaluated, the results are shown in Table S1. It is found that the Pd–Au/SiO_2 is the most excellent catalyst for acetyl oxidation of isobutene. The betterment of catalytic activity comes from synergistic interaction and electronic communications between Pd and Au [37].

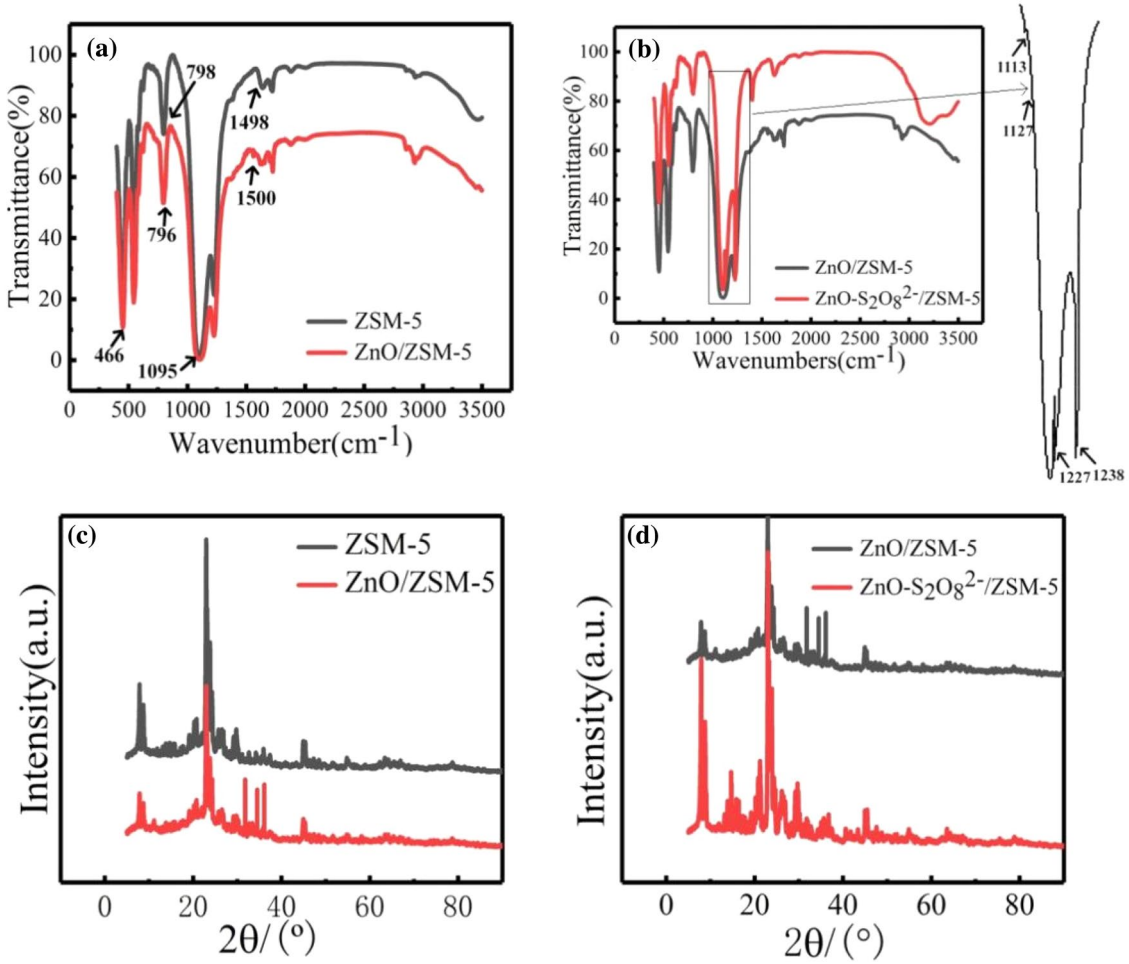

Fig. 4 **a** FT-IR spectra of ZSM-5, ZnO/ZSM-5; **b** FT-IR spectra of ZnO/ZSM-5, ZnO-$S_2O_8^{2-}$/ZSM-5; **c** XRD patterns of ZSM-5, ZnO/ZSM-5; **d** XRD patterns of ZnO/ZSM-5, ZnO–$S_2O_8^{2-}$/ZSM-5

3.2.1 The Effect of Reaction Pressure

The variation of yields along with different reaction pressure is shown in Fig. 6a. The yield of isobutene acetate increased as the reaction pressure passed through a maximum at P = 0.6 MPa and then declined. This implied that when P was below 0.6 MPa, the reaction rate increased with the pressure. Under the lower concentration of O_2 and CH_3COOH, the reaction carried out normally, which is owed to the Pd–Au nano-alloy structure. The nano effect and the alloy structure makes the adsorption–desorption of materials becomes facile [38]. However, when P was above 0.6 MPa, the excessive pressure leads to the liquefaction of isobutene and the formation of vacuoles, which decreases catalytic activity. It indicated that the increasing pressure led to liquefaction of gas phase, which had a significant influence on the gas phase reaction, as has been previously reported [39]. It can found that the optimized reaction pressure is 0.6 MPa.

3.2.2 The Effect of Reaction Temperature

To determine the influence of the reaction temperature, a series of experiments was performed. Figure 6b illustrates that the yield of isobutene acetate increased as the reaction temperature passed through a maximum at T = 160 °C and then declined. It indicates that the increasing temperature contributed to the improving of catalytic activities, which as has been previously reported. Compared with the results of ethylene's acetyl oxidation, the Pd-based catalyst required higher temperature [40]. The introduction of Au and the construction of Pd–Au alloy structure could bring down the activation energy of the reaction [41]. In consequence, the acetyl oxidation could carry out under lower temperature with the Pd–Au nano alloy catalyst. However, when T was above 160 °C, the excessive oxidation reaction leads to the formation of by-products, therefore, which decreased the yield of isobutene acetate. In conclusion, the optimized reaction temperature is 160 °C.

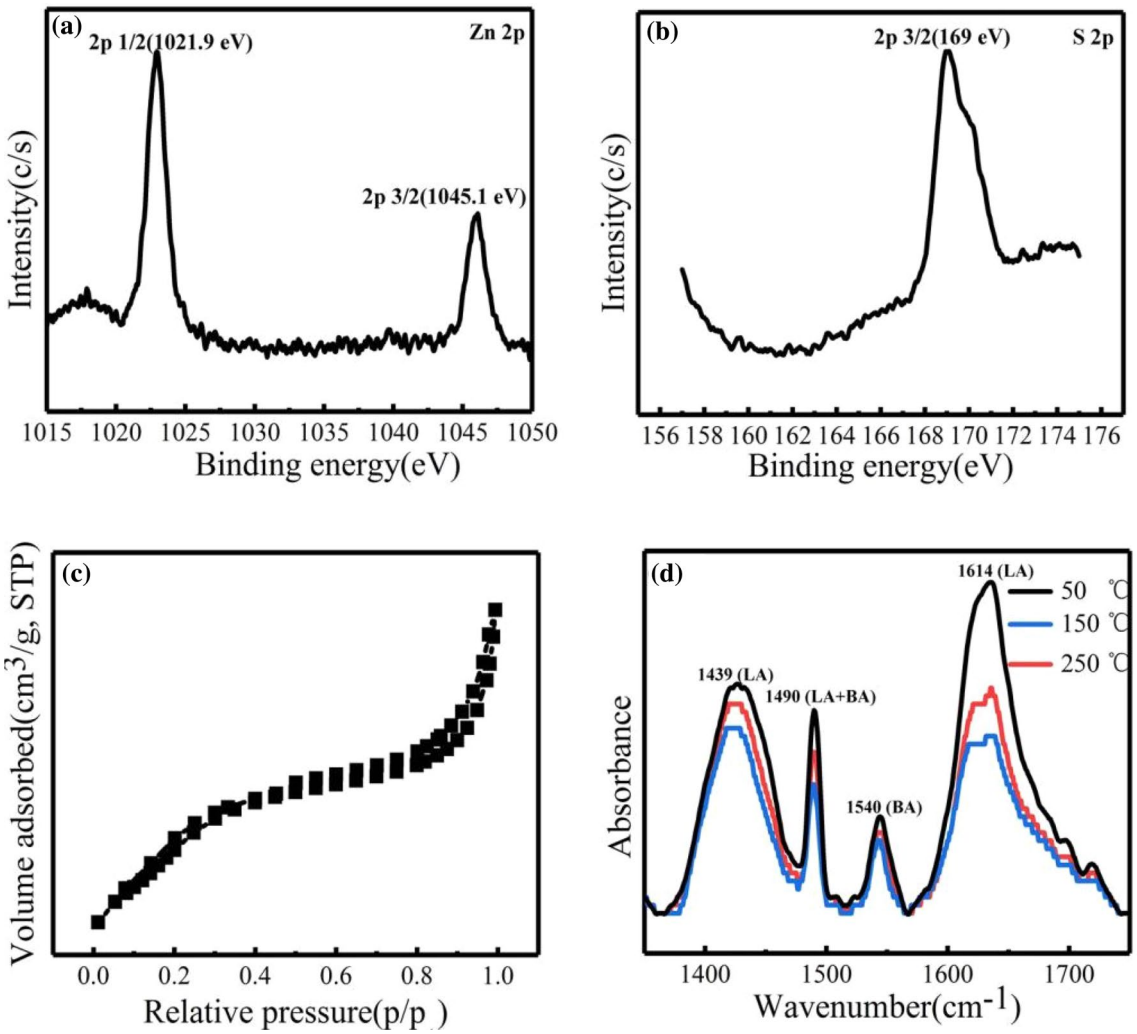

Fig. 5 Zn 2p (**a**) and S 2p (**b**) XPS spectrum of ZnO–$S_2O_8^{2-}$/ZSM-5; **c** N_2 adsorption–desorption isotherms of ZnO–$S_2O_8^{2-}$/ZSM-5; **d** the pyridine-IR spectra of ZnO–$S_2O_8^{2-}$/ZSM-5

Table 1 BET surface area, textural data for ZSM-5, ZnO–$S_2O_8^{2-}$ and ZnO–$S_2O_8^{2-}$/ZSM-5

Sample	A_{BET} (m^2/g)	V_p (cm^3/g)	D (nm)
ZnO–$S_2O_8^{2-}$	4.01	0.01	7.21
ZnO–$S_2O_8^{2-}$/ZSM-5	121.35	0.05	4.47
ZSM-5	320.86	0.12	4.63

A_{BET} BET surface area, *Vp* pore volume, *D* pore size

3.2.3 The Effect of Oxygen Concentration

The change of yields along with different oxygen concentration is shown in Fig. 6c. The alloy structure makes the adsorption–desorption of oxygen on the catalyst's surface easy, as mentioned above. Therefore, the acetyl oxidation of isobutene could carry out regularly under the lower oxygen concentration. The data obtained showed that the yield of isobutene acetate increased as the enhancement of the oxygen concentration. Taking account into the limit of explosion, the oxygen concentration is no more than 6%. Above all, the optimized oxygen concentration is 6%.

3.2.4 The Effect of Acetic Acid Content

The effect of the acetic acid content on the yield of isobutene acetate is then studied, while the results are illustrated in Fig. 6d. The yield of the isobutene acetate increased as the enhancement of the acetic acid content. However, the yield of isobutene acetate is not the highest when the reaction system is all acetic acid (no water is involved in the reaction). The main reason may be that the carbon chains containing more than four carbons tend to produce carbon deposits when they participate in chemical reactions, especially

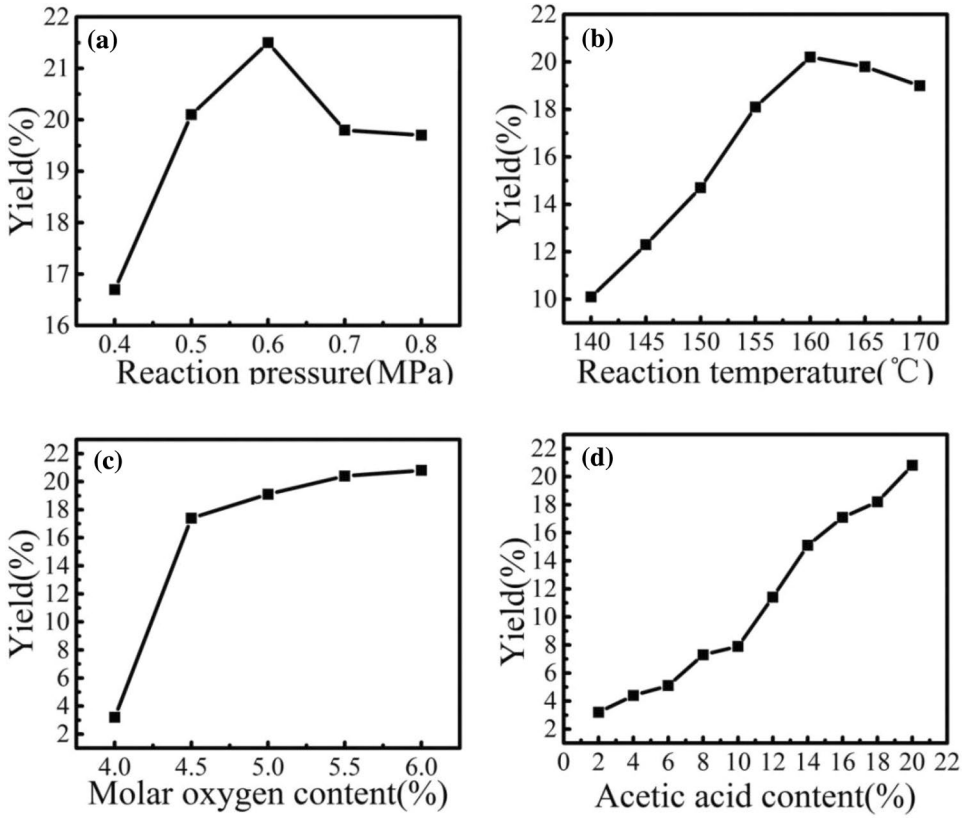

Fig. 6 **a** Influence of reaction pressure, catalyst (100 mg), isobutene (2.30 g, 41 mmol), acetic acid (0.36 g, 6 mmol), oxygen (5 mmol), nitrogen (35 mmol), 160 °C; **b** Influence of reaction temperature, catalyst (100 mg), isobutene (2.30 g, 41 mmol), acetic acid (0.36 g, 6 mmol), oxygen (5 mmol), nitrogen (35 mmol), 0.6 MPa; **c** Influence of oxygen content, isobutene (2.30 g, 41 mmol), acetic acid (0.36 g, 6 mmol), nitrogen (35 mmol), 0.6 MPa, 160 °C; **d** Influence of acetic acid content, isobutene (2.30 g, 41 mmol), oxygen (5 mmol), nitrogen (35 mmol), 0.6 MPa, 160 °C

oxidation reactions. Therefore, the introduction of water component in the reaction system can help to clean up the carbon deposition in the catalyst phase at the same time of the reaction, and has a positive effect on delaying the activity of the catalyst. It could be concluded that the optimized acetic acid content is 20%.

3.2.5 The Stability of Catalyst

The continuous isobutene acetyl oxidation was run for 100 h to investigate the reusability of the conducting reaction in the system (The result is shown in Fig. S1) After 100 h of operation, the yield of isobutene acetate remains at 20.2%. The excellent stability is attributed to the core–shell structure of Pd–Au/SiO_2, the core–shell structure could act as a protective layer on the surface of nanoparticles to improve the stability of catalyst [42]. This result indicates that the Pd–Au/SiO_2 exhibited a good stability and can be used in industrial application widely.

Above all, we obtained encouraging experimental results with 100 conversion and 22% selectivity. We explored the reaction furthermore by mother liquor analysis (The results are shown in Fig. S2, S3). The molecular kinetic diameter of isobutene is larger than ethylene and propylene, so it is difficult for the isobutene to adsorb on the catalyst surface. In addition, isobutene concludes double activity methyl group, which could react with O_2, CH_3COOH independently to generate target material—isobutene acetate, or they are both react with O_2, CH_3COOH to generate main by product—isobutene diacetate. In addition, isobutene reacts with H_2O to generate a handful of isobutenol.

3.3 Synthesis of Methallyl Alcohol

Table 2 lists the yields of 2a for the hydrolysis of 1a (1 mmol) with H_2O (1 mL) for 20 h in the presence of 10 mg of the catalysts. We can find that the thermal reaction showed no conversion of 1a without catalyst (entry 1). The ion exchange resin reported in earlier studies for this reaction [43, 44] showed low yields of 32%. The activity of Y-zeolite and ZSM-5 depended on the Si/Al ratio, and the zeolites with higher Si/Al values, ZSM-5 showed 66% yield. It is significant to note that ZSM-5 shows higher yield than H_2SO_4 and H_3PO_4. Under the same weight conditions, which is a rare example of a heterogeneous catalyst with higher activity (per catalyst weight) than the conventional Brønsted acid for hydrolysis of esters. Non-zeolitic metal oxide (entry 5) showed medium catalytic activity. $S_2O_8^{2-}$/SBA-15 performances higher activity, which inspires our interest. We modified the ZSM-5 by the introduction of Zn^{2+} and $S_2O_8^{2-}$, the result of catalytic activity is listed in Table 3.

Table 2 Catalyst screening hydrolysis of isobutene acetate

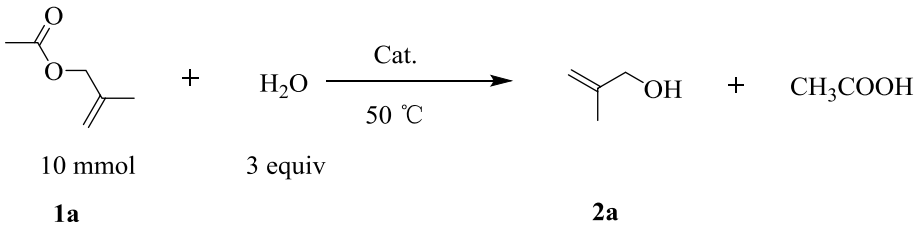

Entry	Catalyst	Conv. (%)	Yield (%)[a]
1	Blank	0	0
2	Ion exchange resin	97.98	31.72
3	H_2SO_4	93.37	34.36
4	H_3PO_4	100	51.89
5	ZnO	47.83	21.37
6	ZSM-5 (Si/Al = 50)	95.61	65.65
7	Y-zeolite (Si/Al = 30)	94.57	8.12
8	Titanium–silica zeolite	82.13	35.67
9	$S_2O_8^{2-}$/SBA-15	100	81.23

[a]GC yields

Table 3 Comparison of catalytic activity

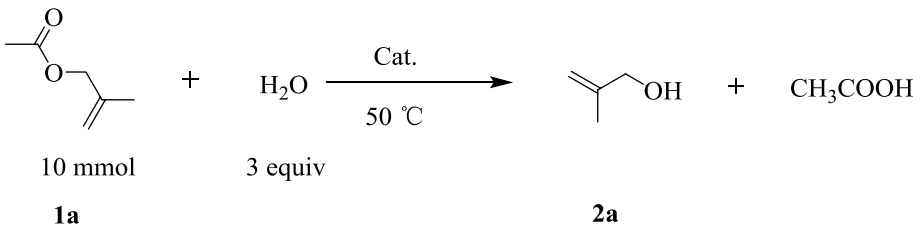

	ZSM-5	ZnO/ZSM-5	ZnO–$S_2O_8^{2-}$/ZSM-5
Conversion (%)	95.61	100	100
Yield (%)	65.65	71.23	100

The results showed that the introduction of Zn^{2+} and $S_2O_8^{2-}$ enhanced the catalytic activity of ZSM-5. We can find that the isobutene acetate is concluded of O–C=O and C=C double bonds. In the presence of H_2O, C=O bond would contend with C=C bond. As unexpected, the C=C reacts with H_2O to produce by-products. The ZSM-5 possess the nature of shape selective catalysis, which reduces markedly the probability that the C=C bond reacts with H_2O. Based on the shape selective catalysis, we modified the function of ZSM-5 [45]. Solid superacids have received our interest due to their strong acidity, ease of separation and stability. The electronic effect of Zn could significantly enhance the catalytic performance. Summarizing the results in Tables 2 and 3, it could be concluded that the catalysts of higher activity have three properties: (1) high Si/Al ratio, (2) three-dimensional large pore structure, (3) strong Brønsted acid sites. The introduction of Zn^{2+} and $S_2O_8^{2-}$ for ZSM-5 meet with the requirements.

3.3.1 The Effect of Reaction Temperature

Figure 7a shows the influence of temperature for the isobutene acetate hydrolysis. The conversion and selectivity increased as the temperature passed through a maximum at T = 50 °C and then declined. The introduction of Zn^{2+} and three-dimensional large pore structure make the isobutene acetate react with the H_2O becoming easier, so the reaction requires lower temperature. It suggested that when T was below 50 °C, the reaction rate is placid. However, when T was above 50 °C, the conversion and selectivity is declined probably due to the reverse esterification of isobutene acetate. It could be seen that the optimized reaction temperature is 50 °C.

3.3.2 The Effect of Catalyst Amounts

The conversion and selectivity along with different catalyst amounts are shown in Fig. 7b. The data obtained showed that the conversion and selectivity increased as the enhancement of catalyst amounts. Based on the Py-IR spectra, it is found that ZnO–$S_2O_8^{2-}$/ZSM-5 provides strong Brønsted acid sites (Fig. 5d). The hydrolysis of isobutene acetate needs the acid condition, the ZnO–$S_2O_8^{2-}$/ZSM-5 could meet with the requirement. When catalyst amounts is 6%, the conversion and selectivity is the peak. Considering the economical efficiency, the optimized catalysts amounts is 6%.

3.3.3 The Effect of Reaction Time

Figure 7c showed the transformation of conversion and selectivity along with the reaction time. The reaction easily achieved a conversion and selectivity of 100% after 40 min. The ester (oil droplet) was on water, and the solid catalysts were suspended in water during the reaction. When reaction time is blow 40 min, isobutene acetate failed to react adequately with water under catalyst. Compared with other hydrolysis of acetate, the time needs 3 h or longer. The ZnO–$S_2O_8^{2-}$/ZSM-5 employs high Si/Al ratio, three-dimensional large pore structure and strong acid condition, which shortens the reaction time of hydrolysis. It could be found that the optimized reaction is 45 min.

3.3.4 The Reusability of Catalyst

As the reusability is a significant factor influencing the practical applications of the catalyst, we carried out a seven run test over the ZnO–$S_2O_8^{2-}$/ZSM-5 under the optimized reaction conditions to evaluate the stability of the catalyst. As is shown in Fig. 7d, the yield of methallyl alcohol remained at 99.5% in the 35 h over the ZnO–$S_2O_8^{2-}$/ZSM-5. The

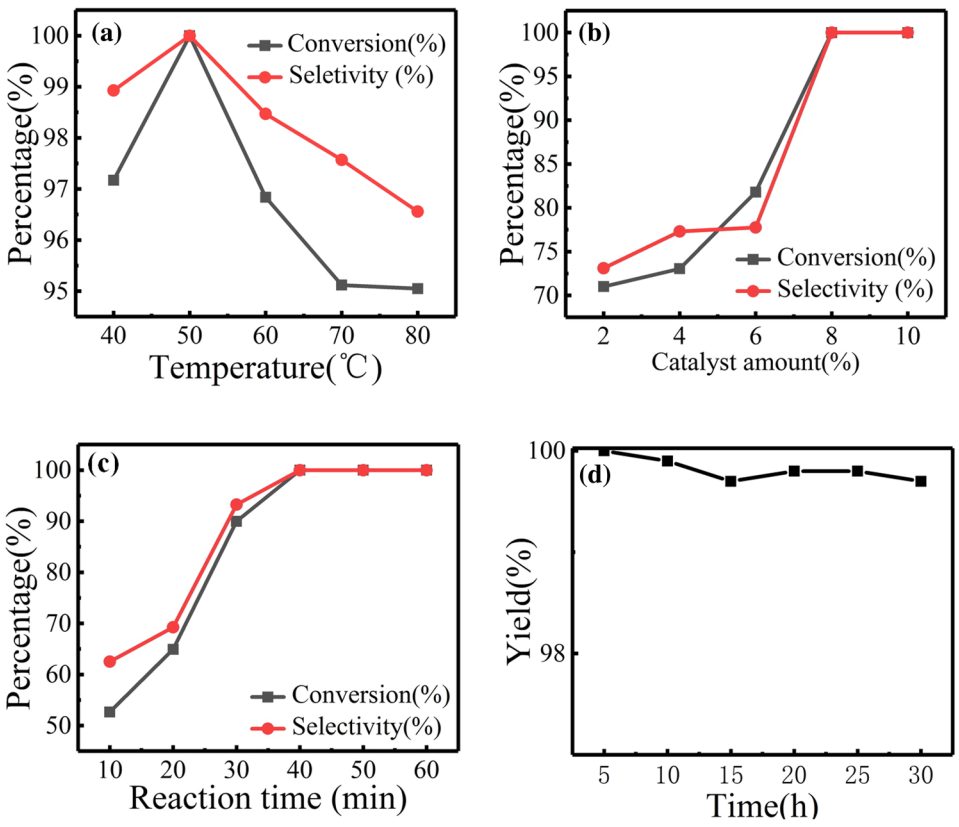

Fig. 7 **a** Influence of reaction temperature, catalyst (10.0 mg), isobutene acetate (0.114 g, 1 mmol), H_2O (1.0 mL), 3 h; **b** Influence of catalyst amount (mass percent of isobutene acetate), isobutene acetate (0.114 g, 1 mmol), H_2O (1.0 mL), 3 h, 50 °C; **c** Influence of reaction time, catalyst (10.0 mg), isobutene acetate (0.114 g, 1 mmol), H_2O (1.0 mL), 50 °C; **d** Catalytic reusability of ZnO–$S_2O_8^{2-}$/ZSM-5, catalyst (10.0 mg), isobutene acetate (0.114 g, 1 mmol), H_2O (1.0 mL), 50 °C, 3 h

$ZnO–S_2O_8^{2-}$/ZSM-5 has the characters of large pore structure and metallic oxide, which enables the catalyst keeping outstanding stability. Compared with the fresh catalyst, a obsolete decline in the yield. The result indicates that the $ZnO–S_2O_8^{2-}$/ZSM-5 performed a better stability and could potentially by used in industrial applications.

4 Conclusions

The core–shell Pd–Au bimetallic nanocrystals supported on SiO_2 are synthesized by the constant volume impregnation method, and the tandem reaction concluding α-H oxidation and esterification oxidation of isobutene is carried out with the catalyst successfully. We investigate the effects of reaction pressure, reaction temperature, oxygen concentration, and the acetic acid content on the acetyl oxidation of isobutene. We conclude that the optimized reaction conditions are 0.6 MPa, 160 °C, oxygen concentration is 6%, acetic acid content is 20%. We develop homodispered $ZnO/S_2O_8^{2-}$ nanoparticles supported on ZSM-5 ($ZnO–S_2O_8^{2-}$/ZSM-5) by ultrasonic adsorption method, and the catalyst exhibits excellent hydrolysis performance of isobutene acetate with 100% conversion and 100% selectivity than H_2SO_4, other Brønsted acid and other catalysts. Furthermore, the catalyst could achieve the strategy of sustainable development and circular economy and sustainable: acetic acid and H_2O could be recycling. This study suggests that Olefin acetyl oxidation-hydrolysis process is a promising green and sustainable method for producing methallyl alcohol in the industries.

Acknowledgement The authors are thankful for the financial support from the National Key Research and Development Program of China (2016YFB0301703).

References

1. Svensson N, Funck EK (2019) Management control in circular economy. Exploring and theorizing the adaptation of management control to circular business models. J Clean Prod 233:390–398
2. Unal E, Shao J (2019) A taxonomy of circular economy implementation strategies for manufacturing firms: analysis of 391 cradle-to-cradle products. J Clean Prod 212:754–765
3. Kinnunen PHM, Kaksonen AH, Gardetti MA (2019) Towards circular economy in mining: opportunities and bottlenecks for tailings valorization. J Clean Prod 228:153–160
4. Wróblewska A, Rzepkowska M, Milchert E (2005) Epoxidation of methallyl alcohol with hydrogen peroxide over TS-1 catalyst. Appl Catal 294:244–250
5. Scrivanti A, Bertoldini M, Beghetto V, Matteoli U (2008) Arylation of β-methallyl alcohol catalyzed by $Pd(OAc)_2$ in combination with $P(t\text{-}Bu)_3$: application to fragrance synthesis. Tetrahedron 64:543–548
6. Ran Q, Zhao H, Shu X, Zhang Q, Yang Y, Liu J, Wu S (2015) Molecular dynamics study of the effects of calcium ions on the conformational properties of comb-like poly(acrylic acid-co-methyl allyl polyoxyethylene ether). Comput Mater Sci 109:90–96
7. Hong L, Zhou N, Fridley D, Raczkowski C (2013) Assessment of China's renewable energy contribution during the 12th five year plan. Energy Policy 62:1533–1543
8. Thomson E (2014) Introduction to special issue: energy issues in China's 12th five year plan and beyond. Energy Policy 73:1–3
9. Lin X, Liao B, Zhang J, Li S, Huang J, Pang H (2019) Synthesis and characterization of high-performance cross-linked polycarboxylate superplasticizers. Constr Build Mater 210:162–171
10. Zhang M, Wu X, Huang X, Yang B, Yu Y (2017) DFT investigations on the conversion of acetylene to undesired vinyl acetylene during vinyl acetate synthesis. Comput Theor Chem 1115:253–260
11. Kuhn M, Jeschke J, Schulze S, Hietschold M, Lang H, Schwarz T (2014) Dendrimer-stabilized bimetallic Pd/Au nanoparticles: preparation, characterization and application to vinyl acetate synthesis. Catal Commun 57:78–82
12. Chu Q, Chen J, Hou W, Yu H, Wang P, Liu R, Song G, Zhu H, Zhao P (2018) Enhancement of catalytic activity by homo-dispersing $S_2O_{82}–Fe_2O_3$ nanoparticles on SBA-15 through ultrasonic adsorption. Chin J Catal 39:955–963
13. Li P, Liu C, Zhang L, Zheng S, Zhang Y (2017) Enhanced boron adsorption onto synthesized MgO nanosheets by ultrasonic method. Ultrason Sonochem 34:938–946
14. Geerken T, Schmidt J, Boonen K, Christis M, Merciai S (2019) Assessment of the potential of a circular economy in open economies-case of Belgium. J Clean Prod 227:683–699
15. Virtanen M, Manskinen K, Uusitalo V, Syvanne J, Cura K (2019) Regional material flow tools to promote circular economy. J Clean Prod 235:1020–1025
16. Karatas Y, Bulut A, Yurderi M, Ertas IE, Alal O, Gulcan M, Celebi M, Kivrak H, Kaya M, Zahmakiran M (2016) Pd–Au–MnO_x nanoparticles supported on amine-functionalized SiO_2 for the room temperature dehydrogenation of formic acid in the absence of additives. Appl Catal B 180:586–595
17. Zhang Z, Zhang L, Yao S, Song X, Huang W, Yan N (2019) Support—dependent rate-determining step of CO_2 hydrogenation to formic acid on metal oxide supported Pd catalysts. J Catal 376:57–67
18. Li J, Wang L, Zhang D, Qian J, Liu L, Xing J (2019) Effect of ZSM-5 acid modification on aromatization performance of methanol. J Fuel Chem Technol 47:957–963
19. Yeh Y, Rzepa C, Rangarajan S, Gorte RJ (2019) Influence of brønsted-acid and cation-exchange sites on ethene adsorption in ZSM-5. Micropor Mesopor Mater 284:336–342
20. Ahn S, Nara H, Yokoshima T, Momma T, Osak T (2019) Effect of enhanced structural stability of Si-O-C anode by carbon nanotubes for lithium-ion battery. Mater Lett 245:200–203
21. Manoilova OV, Olindo R, Areán CO, Lercher JA (2007) Variable temperature FTIR study on the surface acidity of variously treated sulfated zirconias. Catal Commun 8:865–870
22. Chen P, Du M, Lei H, Wang Y, Zhang G, Zhang F, Fan X (2012) SO_4^{2-}/ZrO_2-titania nanotubes as efficient solid superacid catalysts for selective mononitration of toluene. Catal Commun 18:47–50
23. Yang H, Zhuang S, Hu Q, Hu L, Yang L, Au C, Yi B (2018) Competitive reactions of hydroxyl and sulfate radicals with sulfonamides in $Fe^{2+}/S_2O_8^{2-}$ system: reaction kinetics, degradation mechanism and acute toxicity. Chem Eng J 339:32–41
24. Wang H, Shi G, Yu F, Li R (2016) Mild synthesis of biofuel over a microcrystalline $S_2O_8^{2-}/ZrO_2$ catalyst. Fuel Process Technol 145:9–13
25. Wang J, Pan H, Wang A, Tian X, Wu X, Wang Y (2015) Synthesis and characterization of $S_2O_8^{2-}/ZnFe_xAl^{2-}xO_4$ solid acid catalysts for the esterification of acetic acid with n-butanol. Catal Commun 62:29–33

26. Zhao Q, Meng S, Wang J, Li Z, Liu J, Guo Y (2014) Preparation of solid superacid $S_2O_8^{2-}/TiO_2^{-}$exfoliated graphite (EG) and its catalytic performance. Ceram Int 40:16183–16187
27. Moussa OB, Borghol I, Hu D, Casale S, Millot Y, Sayag C, Blanchard J, Durupthy O (2019) Synthesis of supported ZSM-5 nanoparticles. Micropor Mesopor Mater 287:177–182
28. Hou X, Qiu Y, Tian Y, Diao Z, Zhang X, Liu G (2018) Reaction pathways of n-pentane cracking on the fresh and regenerated Sr, Zr and La-loaded ZSM-5 zeolites. Chem Eng J 349:297–308
29. Sharma HK, Archana R, Sankarganesh R, Singh BP, Ponnusamy S, Hayakawa Y, Muthamizhchelvan C, Raji P, Kim DY, Sharma SK (2019) Substitution of Al^{3+} to Zn^{2+} sites of ZnO enhanced the photocatalytic degradation of methylene blue under irradiation of visible light. Solid State Sci 94:45–53
30. Zhang Y, Liu L, Bruggen BV, Leung MKH, Yang F (2019) A free-standing 3D nano-composite photo-electrode-Ag/ZnO nanorods arrays on Ni foam effectively degrade berberine. Chem Eng J 373:179–191
31. Son D, Moon BJ, Lee A, Rho H, Lee HJ, Kim T, Ha J, Lee SH (2019) Polarity effects of ZnO on charge recombination at CsPbBr 3 nanoparticles/ZnO interfaces. Appl Surf Sci 483:165–169
32. Maheswari BU, Sivakumar VM, Thirumarimurugan M (2019) Synthesis, characterization of modified nanoadsorbents and its application in removal of Zn^{2+} ions from battery effluent. J Environ Chem Ecotoxicol 1:2–11
33. Song H, Zhao L, Wang N, Li F (2016) Preparation and chiral recognition ability of chiral stationary phase based on immobilized polyacrylamide derivative. Appl Catal A 526:37–44
34. Zhou S, Sheng W, Wang Z, Yao W, Huang H, Wei Y, Li R (2019) Quick image analysis of concrete pore structure based on deep learning. Constr Build Mater 208:144–157
35. Krishna V, Naresh G, Kumar VV, Sarkari R, Padmasri AH, Venugopal A (2016) Synthesis of 2,6-dimethylpyrazine by dehydrocyclization of aqueous glycerol and 1,2-propanediamine over CuCrO catalyst: rationalization of active sites by pyridine and formic acid adsorbed IR studies. Appl Catal B 193:58–66
36. Han T, Ding S, Yang W, Jönssona P (2019) Catalytic pyrolysis of lignin using low-cost materials with different acidities and textural properties as catalysts. Chem Eng J 373:846–856
37. Shao M, Odell JH, Peles A, Su D (2014) The role of transition metals in the catalytic activity of Pt alloys: quantification of strain and ligand effects. Chem Commun 50:2173–2176
38. Yu W, Porosoff MD, Chen JG (2012) Review of Pt-based bimetallic catalysis: from model surface to supported catalysts. Chem Rev 112:5780–5817
39. Kim D, Won Y, Choi JH, Joo J (2019) Effect of pressure on transport velocity in gas fluidized-beds. Adv Powder Technol 30:2076–2082
40. Liu S, Wang S, Jiang Y, Zhao Z, Jiang G, Sun Z (2019) Synthesis of Fe_2O_3 loaded porous g-C_3N_4 photocatalyst for photocatalytic reduction of dinitrogen to ammonia. Chem Eng J 373:572–579
41. Strasser P, Koh S, Anniyev T, Greeley J, More K, Yu C, Liu Z, Kaya S, Nordlund D, Ogasawara H, Toney MF, Nilsson A (2010) Lattice-strain control of the activity in dealloyed core-shell fuel cell catalysts. Nat Chem 2:454–460
42. Bian Z, Suryawinata IY, Kawi S (2016) Highly carbon resistant multicore-shell catalyst derived from Ni-Mg phyllosilicate nanotubes@silica for dry reforming of methane. Appl Catal B 195:1–8
43. Okuyama K, Chen X, Takata K, Odawara D, Suzuki T, Nakata S, Okuhara T (2000) Water-tolerant catalysis of a silica composite of a sulfonic acid resin. Appl Catal A 190:253–260
44. Siddiki SMAH, Toyao T, Kon K, Touchy AS, Shimizu K (2016) Catalytic hydrolysis of hydrophobic esters on/in water by high-silica large pore zeolites. J Catal 344:741–748
45. Corregidor PF, Cuesta PM, Acosta DE, Destefanis HA (2019) Composite ZSM-5/MCM-41 material obtained from a green resource and its enhanced catalytic performance in the reaction of vinyl acetate and isoamyl alcohol. Appl Catal A 587:117262

Affiliations

Fangfang Shang[1] · Qingyan Chu[1] · Haiyu Yang[1] · Haoxuan Yu[1] · Tonghe Diao[1] · Ping Wang[1] · Hui Liu[1] · Ming Wang[1]

✉ Qingyan Chu
chuqy@sdut.edu.cn

✉ Ping Wang
wangping876@163.com

[1] School of Chemistry and Chemical Engineering, Shandong University of Technology, Zibo 255000, China